The Astrophysical Journal, 897:16 (11pp), 2020 July 1 https://doi.org/10.3847/1538-4357/ab9630

Global Energetics of Solar Flares. XI. Flare Magnitude Predictions of the GOES Class

Markus J. Aschwanden
Solar and Stellar Astrophysics Laboratory (LMSAL), Palo Alto, CA 94304, USA; aschwanden@lmsal.com
Received 2020 April 22; revised 2020 May 22; accepted 2020 May 22; published 2020 June 29

Abstract

In this study we determine scaling relationships of observed solar flares that can be used to predict upper limits of the Geostationary Orbiting Earth Satellite (GOES)–class magnitude of solar flares. The flare prediction scheme is based on the scaling of the slowly varying potential energy $E_p(t)$, which is extrapolated in time over an interval of $\Delta t \leqslant 24$ hr. The observed scaling of the dissipated energy $E_{\rm diss}$ scales with the potential field energy as $E_{\rm diss} \propto E_p^{1.32}$. In addition, the observed scaling relationship of the flare volume, $V \propto E_{\rm diss}^{1.17}$, the multi-thermal energy, $E_{\rm th} \propto V^{0.76}$, the flare emission measure (EM) $\propto E_{\rm th}^{0.79}$, the EM-weighted temperature T_w, and the GOES flux, $F_8(t) \propto E_p(t)^{0.92}$, allows us then to predict an upper limit of the GOES-class flare magnitude in the extrapolated time window. We find a good correlation (cross-correlation coefficient (CCC) ≈ 0.7) between the observed and predicted GOES-class flare magnitudes (in 172 X- and M-class events). This is the first algorithm that employs observed scaling laws of physical flare parameters to predict GOES flux upper limits, an important capability that complements previous flare prediction methods based on machine-learning algorithms used in space-weather forecasting.

Unified Astronomy Thesaurus concepts: Solar physics (1476); Solar flares (1496)

1. Introduction

Solar flare predictions, in particular for eruptive events that impact the heliospheric space weather, became an important area of research that may mitigate the health risk of astronauts in space, minimize power plant outages, and safeguard electronic equipment in the near-Earth space environment. An early warning system that could make short-term predictions within a timescale of 24 hr would be desirable. For the development of such a prediction tool, we have to ask the question: What are the most important physical parameters that facilitate the prediction of energies dissipated in solar flares and space-weather events? Observables used for previous flare prediction methods include: the modified Zurich sunspot classification, the penumbra type of the largest sunspot, and types of sunspot distributions (Gallagher et al. 2002); high-gradient polarity-separation lines in line-of-sight magnetograms and the unsigned magnetic flux near the polarity-separation lines (Schrijver 2007); the effective connected magnetic field between unipolar magnetic areas in a flux-partitioned magnetogram (Georgoulis & Rust 2007); the length of the (neutral) polarity inversion line, the overall twist and shear of the non-potential magnetic field, and the length segment over which the transverse magnetic field is strong (Falconer et al. 2003); the free magnetic energy (Falconer et al. 2011); the gradient-weighted inversion-line length (Cui et al. 2006; Mason & Hoeksema 2010); the unsigned current helicity, the total magnitude of the Lorenz force, the total photospheric magnetic free energy density, and the total unsigned vertical current (Bobra & Couvidat 2015); the history of prior flaring (Falconer et al. 2012); the combination of ultraviolet (UV) brightenings, soft X-ray data, and vector magnetograph data (Nishizuka et al. 2017); synthesized photospheric and coronal data (Jonas et al. 2018); magnetic helicity injection in active regions (Tiwari et al. 2010); and measures of fractality, multi-fractality, and turbulence (Georgoulis 2012). This large arsenal of observables, which is still not capable of providing a fully satisfactory flare prediction method so far, indicates either that we have not yet identified the most relevant physical parameters, or that the measurement accuracy of the relevant physical parameters is insufficient. In both cases, machine-learning methods may not solve the problem (if the training data set does not contain the most relevant physical parameters), and thus we have to resort to more refined physical models. A benchmark test has been conducted during an inter-agency workshop on "all-clear" forecast, where the performance of a number of existing flare prediction algorithms was compared with common data sets from the Michelson Doppler Imager (Scherrer et al. 1995) on board the Solar and Heliospheric Observatory (Fleck et al. 1995), but it was found that no single method outperformed all others, similarly to the situation in climatological forecasting (Barnes et al. 2016).

In this study we develop a flare prediction method that is based on scaling relationships between magnetic field parameters (potential energy, non-potential energy, free energy, dissipated energy), geometric parameters (flare length scale, flare area, flare volume), temperature parameters (emission measure (EM)–weighted temperature), and energetic parameters (multi-thermal energy, EM, Geostationary Orbiting Earth Satellite (GOES) flux). Most parameters have been previously measured in a series of papers on the global energetics of solar flares and coronal mass ejections, in particular in Paper I (Aschwanden et al. 2014b), Paper II (Aschwanden et al. 2015b), and Paper IX (Aschwanden 2019a). A fundamentally new aspect of this method developed here is the strategy to model the force-free coronal magnetic field with automatically traced coronal loop coordinates (e.g., Aschwanden 2016), which bypasses the problem of the non-force-free photospheric magnetic field that is used in traditional magnetic field extrapolation methods (e.g., Wiegelmann et al. 2006). All of the used observables and scaling relationships are based on data from the Helioseismic and Magnetic Imager (HMI; Scherrer et al. 2012) and the Atmospheric Imaging Assembly (AIA; Lemen et al. 2012) on board the Solar Dynamics Observatory (SDO; Pesnell et al. 2012), and from the GOES (e.g., Lemen et al. 2004).

The contents of this study include a summary of the most relevant observational results (Sections 2.1–2.4), modeling results of flare predictions in terms of GOES-class magnitudes (Section 2.5), a discussion and comparisons with previous flare prediction methods (Section 3), and conclusions (Section 4).

2. Data Analysis and Results

2.1. Previous Observations and Parameter Measurements

We use the same data set of solar flares presented in Paper I (Aschwanden et al. 2014b) and Paper II (Aschwanden et al. 2015b), which includes all M- and X-class flares observed with the SDO (Pesnell et al. 2012) during the first 3.5 yr of the mission (2010 June 1 to 2014 January 31). This selection provides 172 flare events with measurements of magnetic parameters (within a heliographic longitude range of [−45°, +45°], for which magnetic field modeling can be faciliated without too severe foreshortening effects near the solar limb), and 391 flare events for measurements of thermal parameters (for events at all longitudes [−90°, +90°]).

We use the 45 s line-of-sight magnetograms from HMI/SDO and make use of all coronal EUV channels of AIA (Lemen et al. 2012) on board the SDO (in the six wavelengths 94, 131, 171, 193, 211, and 335 Å), which are sensitive to strong iron lines in the temperature range of $T \approx 0.6$–16 MK. The spatial resolution is $\approx 1\farcs6$ ($0\farcs6$ pixels) for AIA, and the pixel size of HMI is $0\farcs5$.

The coronal magnetic field is modeled by using the line-of-sight magnetogram $B_z(x, y)$ from the HMI (Scherrer et al. 2012) and (automatically detected) projected loop coordinates $[x(s), y(s)]$ in each EUV wavelength of AIA. A full 3D magnetic field model $\boldsymbol{B}(x, y, z)$ is computed for each time interval and flare with a cadence of 6 minutes, where the total duration of a flare is defined by the GOES flare start and end times. The size of the computation box amounts to an area with a width and length of 0.5 solar radii in the plane-of-sky, and an altitude range of 0.2 solar radius. The total number of analyzed data includes 2706 HMI images and 16,236 AIA images.

For the data analysis of this study, which is focused on scaling laws of magnetic energies dissipated during flares, we extracted from the previous studies the following observables: the mean non-potential magnetic field strength $B_{\rm np}$, the mean potential field strength B_p, the mean magnetic field component $B_{\rm free}$ associated with the free energy $E_{\rm free}$ (or azimuthal field component B_φ), the flare area A, and the total magnetic energy $E_{\rm diss}$ dissipated during the flare duration. The magnetic parameters $B_{\rm np}$, B_φ, $E_{\rm free}$, $E_{\rm diss}$ are all computed with the vertical-current approximation non-linear force-free field (VCA-NLFFF) code, as described in Papers I and IX. This magnetic field extrapolation code essentially assumes vertical currents at flare locations that are associated with sub-photospheric magnetic field concentrations (e.g., sunspots and smaller magnetic features). A major advantage of this code over traditional NLFFF codes is the capability to measure the current-driven twisting of coronal magnetic field lines, based on automated tracing of coronal loops in AIA images, which, this way, bypasses the non-force-freeness of the photospheric field. The spatial scale L is measured from the area $A = L^2$ of the (time-accumulated) azimuthal magnetic field, i.e., $B_\varphi(x, y) \geqslant 100$ G, after correction of projection effects (Paper I).

The multi-thermal energy $E_{\rm th}$ and mean electron density n_e are obtained from a differential emission measure (DEM) analysis, using the relationship of the total EM with the electron density, i.e., $\mathrm{EM} = n_e^2 V \approx n_e^2 L^3$ (Paper II). The quantities B_φ, L, and n_e are determined at the peak times of the flare EM, while the parameters E_f and $E_{\rm diss}$ are integrated over the flare duration τ.

2.2. Observed Scaling Laws

We quantify an observed solar flare with the observables [E_p, $A_{\rm proj}$, l, b, DEM(T)], where E_p is the potential magnetic energy (integrated over the volume of a computational box that encompasses a flaring active region), $A_{\rm proj}$ is the projected 2D area of the flaring region on the solar surface, l and b are the heliographic longitude and latitude, respectively, and DEM(T) is a DEM distribution.

First we calculate the potential field energy E_p, which can be obtained from a line-of-sight magnetogram $B_z(x, y)$ by means of a standard magnetic (potential) field extrapolation in the 3D volume V of the computation box $[x, y, z]$ that encompasses a flaring active region,

$$E_p = \int \left(\frac{B_p^2(x, y, z)}{8\pi} \right) dV \quad = \int \left(\frac{B_p^2(x, y, z)}{8\pi} \right) dx\ dy\ dz. \tag{1}$$

Note that the potential field energy E_p represents the minimum magnetic energy state, which is a lower limit of the non-potential field (Priest 1975).

In Figure 1(a), we show a linear regression fit to the free energies $E_{\rm free}$ as a function of the potential field energies E_p, computed for 172 GOES X-class and M-class flares using the VCA-NLFFF code, according to the latest version, as described in Paper IX (Figure 8(b) therein). This linear regression fit yields the scaling relationship

$$\left(\frac{E_{\rm free}}{10^{30}\ \mathrm{erg}} \right) = 10^{-1.73} \left(\frac{E_p}{10^{30}\ \mathrm{erg}} \right)^{1.26}. \tag{2}$$

Similarly we show in Figure 1(b) a linear regression fit to the dissipated energies $E_{\rm diss}$ as a function of the potential field energies E_p, as described in Paper IX (Figure 8(c) therein). This linear regression fit yields the scaling relationship

$$\left(\frac{E_{\rm diss}}{10^{30}\ \mathrm{erg}} \right) = 10^{-2.19} \left(\frac{E_p}{10^{30}\ \mathrm{erg}} \right)^{1.32}. \tag{3}$$

We see that these two relationships are similar; in particular, they have a similar power-law slope of $p \approx 1.3$, while the dissipated energy contains about half of the free energy, i.e., $E_{\rm diss} \approx E_{\rm free}/2$. Uncertainties of all linear regression fits are indicated in Figures 1–2 by the mean (thick solid line) and standard deviation of the slopes (thin solid lines).

In the next step, we define the scaling relationships of geometric parameters, such as the flare length scale L, the flare area A, and the flare volume V. We can directly observe the projected flare area $A_{\rm proj}$ only, and estimate the true (unprojected) area A by dividing by the cosine of the longitude l and latitude b difference to disk center,

$$A = \frac{A_{\rm proj}}{\cos \sqrt{l^2 + b^2}}. \tag{4}$$

Note that the observed flare area $A_{\rm proj}$ is measured (in Papers I and II) from the sum of the pixel areas above some threshold of

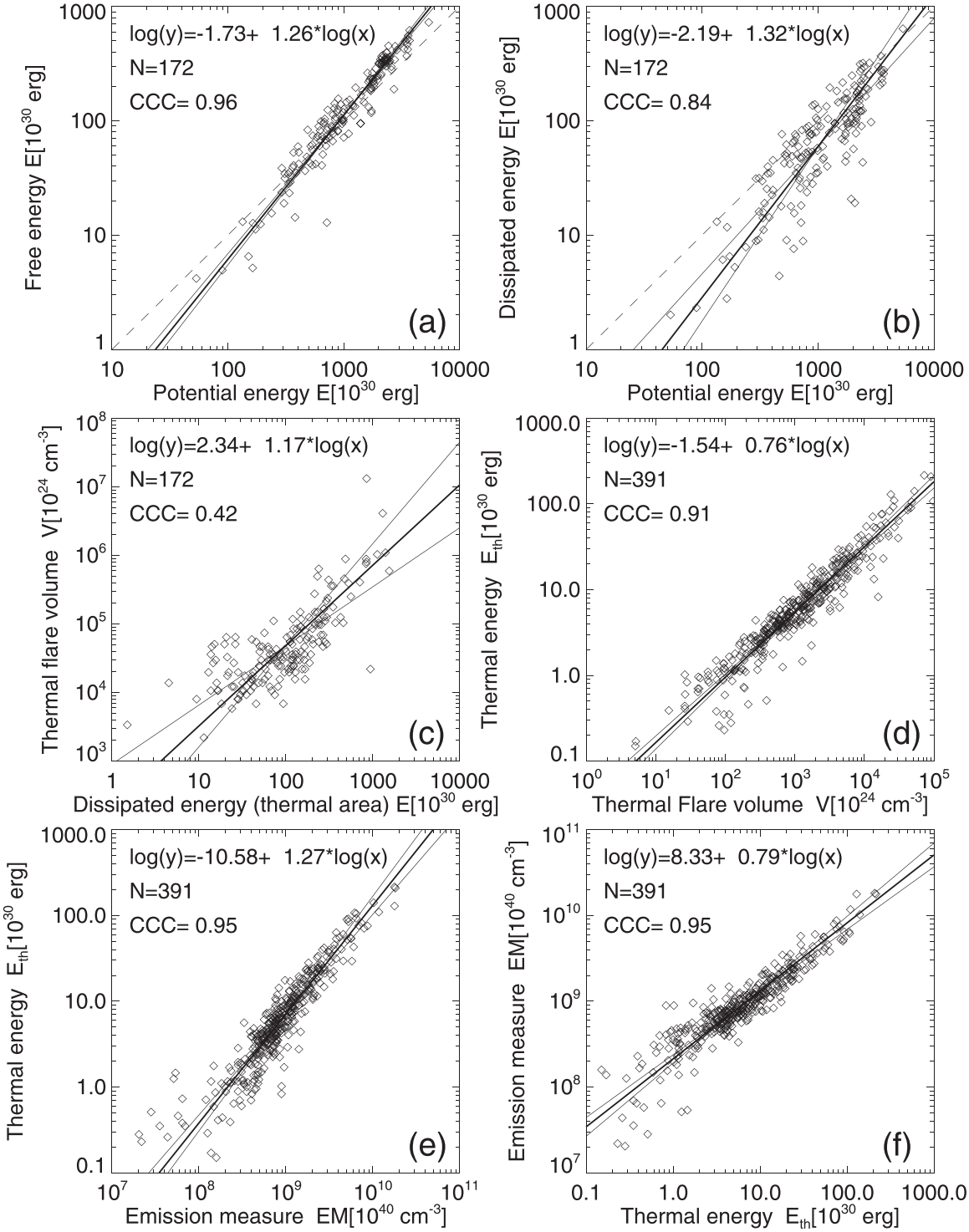

Figure 1. Correlations between the observed values (diamonds) as a function of the potential energy are shown for the free energy (a), the dissipated energy (b), the flare volume (c), the thermal energy (d), and the EM (e and f). Linear regressions are shown for the logarithmic values, with the mean (thick solid lines), standard deviation (thin solid lines), and equivalence (dashed lines) indicated.

the dissipated magnetic flare energy $E_{\rm diss}$. The time dependence of the flare area is taken into account by calculating the cumulative flare area, accumulated between the flare start and end time (Papers I and II). After we have defined the flare area A, we can simply define a flare length scale L by

$$L = A^{1/2}, \tag{5}$$

and a flare volume V by

$$V = A^{3/2}. \tag{6}$$

As a next step, we can investigate the relationship between the dissipated energy $E_{\rm diss}$ and the flare volume V, which is shown in Figure 1(c) (using the parameters determined in Paper I and shown in Figure 14(c) therein). The two parameters exhibit a

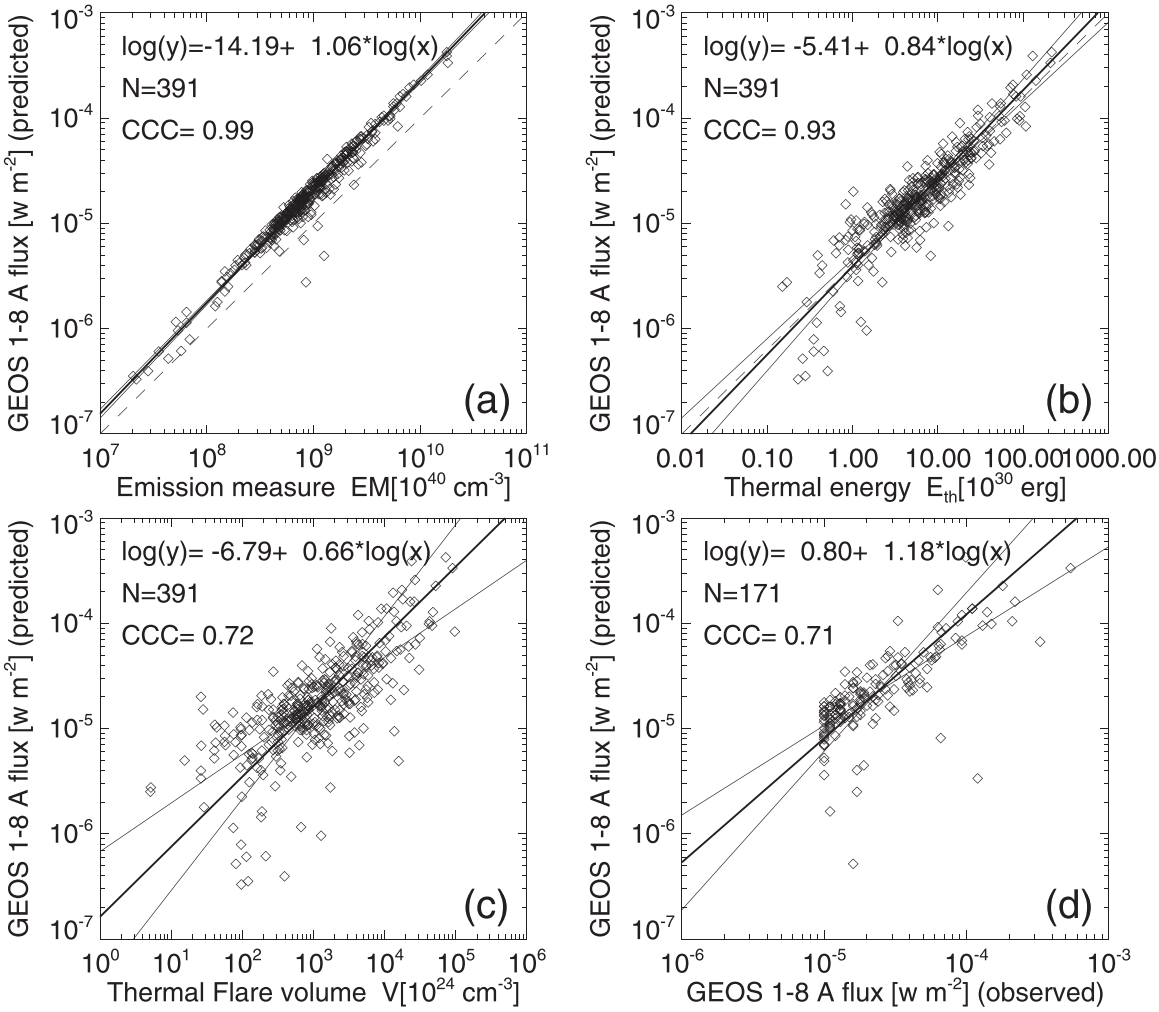

Figure 2. Correlations between the calculated GOES class and the EM (a), the (multi-)thermal energy $E_{\rm th}$ (b), the flare volume V, and the observed GOES class (d). Linear regressions are shown for the logarithmic values, with the means (thick solid lines) and standard deviations (thin solid lines), and equivalence (dashed lines) indicated.

correlation that is fitted by the relationship

$$\left(\frac{V}{10^{24}\ \mathrm{cm}^3}\right) = 10^{2.34}\left(\frac{E_{\rm diss}}{10^{30}\ \mathrm{erg}}\right)^{1.17}, \tag{7}$$

which is almost a linear function.

Since both the flare volume V and the (space-integrated) multi-thermal energy $E_{\rm th}$ have the same volume dependence, we expect a nearly linear relationship. There is indeed a strong correlation between these two parameters (cross-correlation coefficient (CCC) = 0.91), as shown in Figure 1(d) (or Figure 5(b) in Paper II),

$$\left(\frac{E_{\rm th}}{10^{30}\ \mathrm{erg}}\right) = 10^{-1.54}\left(\frac{V}{10^{24}\ \mathrm{cm}^3}\right)^{0.76}. \tag{8}$$

Another volume-dependent quantity is the EM, which is shown in Figure 1(e) (or in Figure 1(f) with reversed axes, as in Paper II, Figure 5(f) therein),

$$\left(\frac{\mathrm{EM}}{10^{40}\ \mathrm{cm}^3}\right) = 10^{8.33}\left(\frac{E_{\rm th}}{10^{30}\ \mathrm{erg}}\right)^{0.79}. \tag{9}$$

Since the DEM is generally a multi-temperature distribution, we define a weighted temperature T_w, using the integral over the function DEM(T),

$$T_w = \frac{\int T \times \mathrm{DEM}(T)\ dT}{\int \mathrm{DEM}(T)\ dT} = \frac{\int T \times \mathrm{DEM}(T)\ dT}{\mathrm{EM}}. \tag{10}$$

The determination of the DEM distributions DEM(T) using AIA/SDO data is described in Paper II and references therein. The main feature of our DEM analysis is the proper treatement of the multi-thermal distribution, rather than the commonly used isothermal approximation. A benchmark test with comparisons of 11 different DEM methods is described in Aschwanden et al. (2015a). In the study here, we distinguish between the (temperature-integrated) $\mathrm{EM}_{\rm AIA}$ calculated from the six coronal AIA channels, and the GOES EM ($\mathrm{EM}_{\rm GOES}$), which is calculated from the isothermal channel ratio of the two GOES wavelength ranges 1–8 and 0.5–4 Å .

2.3. Scaling Law of GOES Flux

We can now use the two parameters [EM,T_w] to predict the GOES fluxes F_4 and F_8 in the wavelength ranges λ = 0.5–4 and 1–8 Å. The original calibration of the GOES fluxes is given in Thomas et al. (1985), and later updated by White et al. (2005). Software capabilities to extract GOES data have been

implemented in the interactive data language (IDL) solar software by Freeland & Handy (1998). We use the calibration of the most recent GOES spacecraft (GOES-12) given in White et al. (2005). GOES data during the SDO era were provided by GOES-15 (launched on 2010 March 4) and by GOES-16 (launched on 2016 November 19). For a given flux ratio R,

$$R = F_4/F_8, \tag{11}$$

the GOES temperature $T_{\rm GOES}$ is given by a third-order polynomial (with the coefficients measured from the most recent GOES satellite (GOES-12) given in that paper),

$$T_{\rm GOES} = 3.90 + 101.2\ R - 266.4\ R^2 + 390.2\ R^3, \tag{12}$$

and the parameter $b_8(T)$ is given by a third-order polynomial also,

$$b_8(T) = -12.31 + 3.75\ T_{\rm GOES} - 0.1003\ T_{\rm GOES}^2 + 0.001195\ T_{\rm GOES}^3, \tag{13}$$

yielding the $\rm EM_{GOES}$,

$$\rm EM_{GOES} = 10^{55}\ F_8/b_8(T). \tag{14}$$

In our application we approximate the $\rm EM_{GOES}$ and temperature $T_{\rm GOES}$ with the AIA-inferred emission measure ($\rm EM_{AIA}$) and EM-weighted temperature T_w. However, in order to allow for different temperature responses of the two instruments AIA and GOES, we define an empirical normalization factor $q_{\rm AIA}$,

$$q_{\rm AIA} = \frac{\rm EM_{GOES}}{\rm EM_{AIA}} \approx 0.54, \tag{15}$$

which we determine by the normalization of the predicted mean value of the GOES flux to the observed value, i.e., $F_8^{\rm pred}/F_8^{\rm obs} = 1.00$ (Figure 3). We can then directly calculate the calibration parameter b_8 (Equation (14)), and predict the GOES long-wavelength flux F_8 by inverting Equation (14),

$$F_8 = \frac{\rm EM_{GOES}\ b_8}{10^{55}} = q_{\rm AIA}\ \rm EM_{AIA}\ b_8\ 10^{-55}. \tag{16}$$

The GOES flux is given in physical units of [W m^{-2}], which scales with the well-known GOES flare classes as $F_8 = 10^{-6}$ [W m^{-2}] for a C1.0-class flare, $F_8 = 10^{-5}$ [W m^{-2}] for an M1.0-class flare, and $F_8 = 10^{-4}$ [W m^{-2}] for an X1.0-class flare.

In Figure 2, we show the resulting correlations of the calculated GOES fluxes F_8 as a function of the EM (Figure 2(a)), which represents the best-correlated parameter (with a CCC = 0.99),

$$\left(\frac{F_8}{\rm W\ m^{-2}}\right) = 10^{-14.19}\left(\frac{\rm EM}{10^{40}\ cm^3}\right)^{1.06}. \tag{17}$$

There are also good correlations of the GOES flux F_8 with the thermal energy $E_{\rm th}$ (Figure 2(b)), with CCC = 0.93,

$$\left(\frac{F_8}{\rm W\ m^{-2}}\right) = 10^{-5.41}\left(\frac{E_{\rm th}}{10^{30}\ erg}\right)^{0.84}, \tag{18}$$

and with the thermal flare volume $V_{\rm th}$, with CCC = 0.72,

$$\left(\frac{F_8}{\rm W\ m^{-2}}\right) = 10^{-6.79}\left(\frac{V_{\rm th}}{10^{24}\ cm^3}\right)^{0.67}. \tag{19}$$

The most important test of our scaling law relationships is the expected correlation between the observed GOES fluxes $F_8^{\rm obs}$ and the predicted values $F_8^{\rm pred}$. Remember that the GOES fluxes F_8 were calculated from the EM and the EM-weighted temperatures T_w (Equations (10)–(15)), which are obtained from the scaling laws of the EM($E_{\rm th}$) (Equation (9)), the (multi-)thermal energy $E_{\rm th}(V)$ (Equation (8)), the flare volume $V(E_{\rm diss})$ (Equation (7)), the dissipated flare energy $E_{\rm diss}(E_p)$ (Equation (3)), and the potential field energy $E_p(B_p)$ (Equation (1)). Thus the final prediction of the GOES fluxes depends ultimately on the potential field $\boldsymbol{B}_p$ only. If our inferred scaling laws are correct, we would expect a close correlation between the observed ($F_8^{\rm obs}$) and the predicted GOES fluxes ($F_8^{\rm pred}$). The analytical derivation of this GOES scaling law is given in the Appendix. We show a cross-correlation plot of these two quantities in Figure 2(d), which reveals a reasonably good CCC = 0.71,

$$\left(\frac{F_8^{\rm pred}}{\rm W\ m^{-2}}\right) = 10^{0.80}\left(\frac{F_8^{\rm obs}}{\rm W\ m^{-2}}\right)^{1.18}. \tag{20}$$

This test establishes our claim that we can predict the GOES class of a flare, based on the potential field alone. Since the temporal evolution of the potential field is generally relatively slow, it provides a robust prediction for the flare magnitude (i.e., GOES class).

In Figure 3, we show the ratios $q_{\rm acc}$ of the predicted $F_8^{\rm pred}$ to the observed GOES values $F_8^{\rm obs}$, which exhibit a Gaussian-like distribution with a mean and standard deviation of $q_{\rm acc} = 1.8 \pm 0.6$, for the 172 flare events investigated in this study. Normalizing the AIA-inferred multi-thermal $\rm EM_{AIA}$ to the GOES-inferred isotherma $\rm EM_{GOES}$, we find a normalization factor of $q_{\rm AIA} = \rm EM_{GOES}/EM_{AIA} = 0.54$, which has a mean and standard deviation of $q_{\rm AIA} = 1.00 \pm 0.40$ (Figure 3) and implies that the accuracy of the GOES scaling laws is $\approx \pm 40\%$.

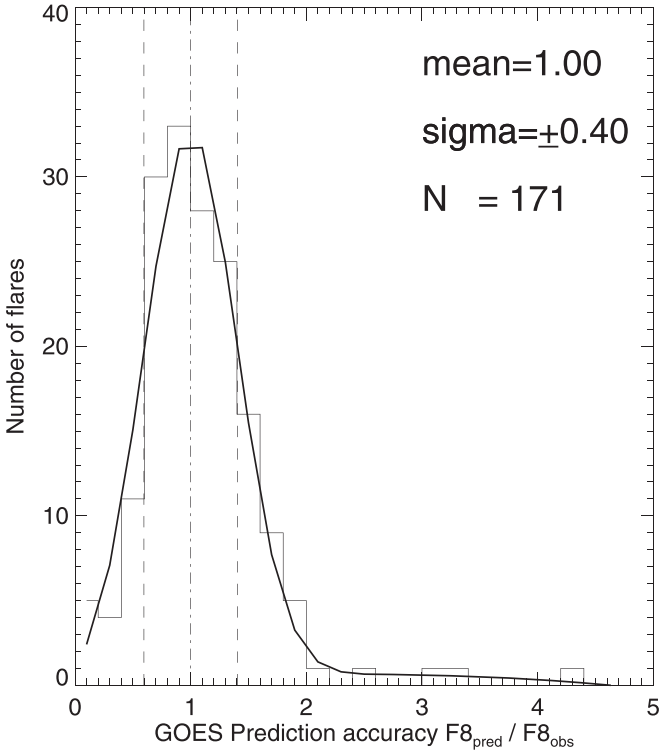

Figure 3. Histogram of the GOES-class prediction accuracy, which is specified by the ratio of $q_{\rm acc} = F8_{\rm pred}/F8_{\rm obs}$ with a mean and standard deviation of $q_{\rm acc} = 1.0 \pm 0.4$, shown as a Gaussian fit.

2.4. Simplified GOES-class Estimates

Our goal is the prediction of the GOES (1–8 Å) flux F_8 for each flare, based on information on the potential field energy E_p. A direct scaling relationship between these two parameters F_8 and E_p can be obtained by combining all Equations (1)–(15),

$$F_8 = q_{\rm AIA}\ b_8(T_w)\ 10^{-8} \left(\frac{E_p}{10^{30}\ {\rm erg}} \right)^{0.92} \quad [{\rm W\ m^{-2}}], \qquad (21)$$

where the detailed analytical derivation is given in the Appendix. Since the EM-weighted temperature in our sample of 172 X- and M-class flare events is relatively narrow, varying only by a factor of ≈20%,

$$T_w \approx 25.5 \pm 5.6\ [{\rm MK}], \qquad (22)$$

we obtain a mean calibration factor $b_8(T_w)$ of

$$b_8(T_w) \approx 38, \qquad (23)$$

which together with the normalization factor $q_{\rm AIA} = 0.54$ yields then the simple scaling law.

$$F_8 \approx 2.05 \times 10^{-7} \left(\frac{E_p}{10^{30}\ {\rm erg}} \right)^{0.92} \quad [{\rm W\ m^{-2}}]. \qquad (24)$$

This simplified scaling law allows for quick estimates of the GOES class. Total (potential field) energies of $E_p \approx 5$, 50, and 500×10^{30} erg are required for flare magnitudes of GOES class C1.0, M1.0, and X1.0. We will use the simplified scaling law of Equation (24) for flare forecasting in the following sections.

2.5. Daily Forecasting of GOES Flare Magnitude

In this section we generate a new data set that produces a time series of magnetic potential field energies $E_p(t)$, using the VCA-NLFFF code. Detailed descriptions of the magnetic field code are given in Aschwanden et al. (2014a) and Aschwanden (2016). We use observations of active regions from HMI/SDO and AIA/SDO during the month of 2011 February 1–28, which we analyze with a cadence of $\Delta t = 24$ hr. The Sun was very active during this month, producing one X2.2 GOES-class flare and 13 M-class flares (Table 1). We use the NOAA flare catalog (hesperia.gsfc.nasa.gov) to identify the heliographic coordinates of the active regions. There are one, none, or multiple active regions present every day, for which we have to calculate magnetic field extrapolations separately, and have to add them up in order to gather all significant magnetic energies on the visible solar disk. For the month of 2011 February, we find a total of 23 days (out of the 28 days) with active regions present, encompassing a total of 53 active regions, according to the NOAA data catalog.

Our main goal is to test whether our anticipated algorithm is able to predict upper limits of the GOES 1–8 Å flux $F_8(t)$ based on the potential magnetic energies only (i.e., using the scaling law $F_8(t) \propto E_p(t)^{0.92}$ (Equation (24)). First we show the obtained time profiles of the potential energy $E_p(t)$ (Figure 4(a)), the non-potential energy $E_{\rm np}(t)$ (Figure 4(b)), and the free energy $E_{\rm free}(t)$ (Figure 4(c)). For comparison we also show the results of an earlier version of the VCA-NLFFF code (noisy time profiles in Figures 4(a) and (b)) for the time segment of 2011 Feburary 12–17 (Aschwanden 2016). The time evolution of the potential and non-potential energy is in good agreement between the old and new version of the VCA-NLFFF code (Figures 4(a) and (b)), while the free energy exhibits slight differences, caused by the fact that the free energy is a small difference of two large quantities, i.e., $E_{\rm free} = E_{\rm np} - E_p$, and thus has a larger relative uncertainty.

We show the GOES 1–8 Å flux time profile in Figure 4(d) (gray area), which contains 14 M- and X-class flare events during the investigated time window of 28 days. First we consider the "now-cast" case, where the predicted time is identical to the observed time. We take the potential field energy $E_p(t)$ and calculate the upper limit of the GOES flux $F_8(t)$ with the scaling law given in Equation (24), i.e., $F_8(t) \propto E_p(t)^{0.92}$ and overplot it on the actually observed GOES 1–8 Å flux in Figure 4(d) (gray area), which demonstrates that the derived GOES fluxes indeed represent reliable upper limits as a function of time. The uncertainty of the empirical scaling law amounts to $q_{acc} = F_8^{\rm pred}/F_8^{\rm obs} = 1.0 \pm 0.4$ (Figure 3). This means that we expect a probability of 67% for one standard deviation ($\sigma = \pm 0.4$).

Next we consider the "flare prediction" case (of the upper limit of the GOES flux $F_8^{\rm pred}(t)$), for a time interval of $\Delta t = 24$ hr ahead of the observing time, which is shown in Figure 4(e) (thick solid line). The predicted value $E_p(t)$ is computed by linear extrapolation from the past two time intervals, i.e., $E_p(t) = 2{*}E_p(t - \Delta t) - E_p(t - 2\Delta t)$, and the empirical scaling law $F_8(t) \propto E_p(t)^{0.92}$ is then applied. To avoid unphysical negative values in the extrapolated potential energy $E_p(t)$, we extrapolate the logarithmic values.

The four largest flares (see Table 1) occurred on 2011 February 13, 15, 18, and 24, with GOES fluxes of M6.6, M2.2, M6.6, and M3.5 (indicated in Figure 4(e)), for which we predict upper limits of M7.3, X1.4, M7.5, and M8.3, corresponding to flux ratios of $q_8 = F_8^{\rm obs}/F_8^{\rm pred} = 0.9$, 1.5, 0.9, and 0.4, respectively, which is approximately consistent with our expectation of $q_{\rm acc} = 1.0 \pm 0.4$ (Figure 3). Both the predicted upper limit of the GOES flux (Figure 4(e), thick curve) and the limit of the now-cast case (Figure 4(e), dashed curve) are shown together in Figure (4)), so that the uncertainty due to the temporal extrapolation can be seen. The comparison corroborates our assumption that the potential energy $E_p(t)$ is relatively slowly varying on a timescale of a day.

3. Discussion

3.1. Physical Parameters Relevant for Flare Prediction

A magnetic potential field represents the minimum energy state (Priest 1975), from which no energy can be dissipated to produce a solar flare. Only the free energy $E_{\rm free} = E_{\rm np} - E_p$, which is the difference between the non-potential field and the potential field energy, can be dissipated in flares, which constrains the choice of valid physical parameters in flare models. A selection of 25 physical parameters that can be measured in active regions has been presented by Bobra & Couvidat (2015), and a subset of 18 parameters thereof in Bobra & Ilionidis (2016), drawn from the Space-weather HMI Active Region Patches (SHARP) project. For flare predictions, however, only those parameters are relevant that are directly sensitive to the free energy $E_{\rm free} > 0$, or to the underlying electric current density $\nabla \times \boldsymbol{B} = 4\pi \boldsymbol{j} = \alpha(\boldsymbol{r})\ \boldsymbol{B}$. In the study of Bobra & Couvidat (2015), we identify 17 relevant physical parameters, which quantify the free energy ($\rho_{\rm tot}$, $\overline{\rho}$), the vertical currents ($J_{z,{\rm total}}$, $J_{z,{\rm sum}}$, $\overline{J_z}$), the helical twist angle ($\alpha_{\rm total}$), the shear angle ($\overline{\Gamma}$), the helicity ($H_{z,{\rm total}}$, $H_{\rm abs}$, $\overline{H_c}$), and the Lorentz force (F, F_z, F_y, F_x, δF_x, δF_y, $v\delta F_z$). The Lorentz force depends

Table 1
Observed and Predicted Upper Limits of the GOES 1–8 Å Flux during the Month of 2011 February 1–28, Containing a Total of 14 X- and M-class Flares

Date Time	Heliographic Position	NOAA	GOES Flux F_8^{obs} (W m^{-2})	Predicted Upper Limit F_8^{pred} (W m^{-2})	Ratio F_8^{obs}/F_8^{pred}
2011 Feb 9 01:23:00	N16W70	11153	M1.9	M1.0	1.9
2011 Feb 13 17:28:00	S21E04	11158	M6.6	M7.3	0.9
2011 Feb 14 17:20:00	S20W07	11158	M2.2	X1.1	0.2
2011 Feb 15 01:44:00	S21W12	11158	X2.2	X1.4	1.5
2011 Feb 16 01:32:00	S22W27	11158	M1.0	M7.7	0.1
2011 Feb 16 07:35:00	S23W30	11161	M1.1	M6.7	0.2
2011 Feb 16 14:19:00	S23W33	11158	M1.6	M5.8	0.3
2011 Feb 18 09:55:00	S21W55	11158	M6.6	M7.5	0.9
2011 Feb 18 10:23:00	N17E07	11162	M1.0	M7.4	0.1
2011 Feb 18 12:59:00	S20W70	11158	M1.4	M7.2	0.2
2011 Feb 18 14:00:00	N17E04	11162	M1.0	M7.1	0.1
2011 Feb 18 20:56:00	N15E00	11162	M1.3	M6.4	0.2
2011 Feb 24 07:23:00	N14E87	11163	M3.5	M8.3	0.4
2011 Feb 28 12:38:00	N22E35	11164	M1.1	M1.0	1.1

on the free energy component $B_{\rm free}$ only, i.e., $\boldsymbol{F} \propto \boldsymbol{j} \times \boldsymbol{B}_{\rm np} = \boldsymbol{j} \times \boldsymbol{B}_p + \boldsymbol{j} \times \boldsymbol{B}_{\rm free} = \boldsymbol{j} \times \boldsymbol{B}_{\rm free}$, since there is no current in the potential field. The other forthcoming parameters are sensitive to the non-potential magnetic field strength $\boldsymbol{B}_{\rm np} = [B_x, B_y, B_z]$, rather than to the magnetic field component associated with the free energy, i.e., $\boldsymbol{B}_{\rm free} = \boldsymbol{B}_{\rm np} - \boldsymbol{B}_p$. The remaining parameters, such as the magnetic flux (Φ, Φ_R), the flare area (A, A_{45}), the field divergence ($\overline{\nabla B_{\rm tot}}$, $\overline{\nabla B_z}$, ∇B_h), or the inclination angle $\overline{\gamma}$, are thus not directly relevant for flare predictions, although they may be useful in characterizing (non-flaring) active regions.

3.2. Flare Prediction Algorithms

Early flare prediction algorithms were based on empirical (morphological) parameters rather than physical models. For instance, Gallagher et al. (2002) developed a flare prediction system that estimates the probability for each active region to produce C-, M-, or X-class flares based on sunspot classification.

With increasing sophistication, a trend from morphological parameters to physical parameters took place, mostly measured from line-of-sight magnetograms. For instance, a method of partitioning the magnetic flux in a magnetogram and deriving the magnetic connectivity has been used in forecasting of major flares (Barnes et al. 2005; Georgoulis & Rust 2007). The lower moments of the field gradients, the kurtosis of the vertical-current density, the magnetic twist, the current helicity density, and the magnetic shear angle have been used in another series of studies (Leka & Barnes 2003, 2007; Barnes et al. 2007; Barnes & Leka 2008). It was noted that parameters that depend on the size of a flare are better correlated with the flaring behavior than parameters that do not depend on the system size (Welsch et al. 2009), which is consistent with our definition of the behavior of the free energy, which is spatially integrated over the entire flaring active region and thus depends on the system size.

Ultimately we aim to find physical flare models that can predict the onset of a flare instability, if solar flares are produced by a deterministic process. However, many studies show that flaring appears to be a stochastic process, which cannot predict individual flares, rather than a deterministic process. Neverthelss, flare forecasting has been approached by machine-learning algorithms (e.g., Bobra & Couvidat 2015; Bobra & Ilionidis 2016), which optimize prediction skills, regardless of whether the flare process is stochastic or deterministic. The algorithm of Bobra & Couvidat (2015) is based on binary classifiers, where an active region belongs to a positive class if it produces one or more flares within a given time interval, and conversely, an active region belongs to a negative class if it does not produce a flare in the same time interval. This is slightly different from our method with one qualifier, where only an upper limit of a flare magnitude is predicted within a time window in the near future. Thus, we do not predict the actual time when a flare occurs, but only an upper limit in case a flare occurs. This relieves also the class-imbalance problem (Bobra & Couvidat 2015). In our method we can identify two types of uncertainties: (i) the error of the theoretical scaling law (which can be measured from the difference of theoretical and observational values at now-cast time $t = t_{\rm now}$), and (ii) the time extrapolation error (which can be measured from the difference in the prediction time window, at ($t > t_{\rm now}$)). From the 25 physical parameters tested in Bobra & Couvidat (2015), we identify 17 relevant physical parameters that are sensitive to the free energy, the vertical current, the helical twist angle, the shear angle, or helicity, in agreement with our physical model of the vertical-current approximation (VCA) NLFFF code. The underlying physical model is essentially a force-free solution of helically twisted magnetic field lines, which are generated by vertical currents emanating above (sub-photospheric) magnetic flux concentrations. If this physical model is correct, we expect that these physical parameters have a relatively high prediction score, which is indeed largely the case. However, the observables in the study of Bobra & Couvidat (2015) are based on photospheric magnetograms, which are not force-free (Metcalf et al. 1995), while the magnetic parameters in this study are derived with the VCA-NLFFF code by fitting of coronal loops, which are thought to be force-free (with a plasma-β-parameter $\beta \ll 1$), and thus are expected to provide a more realistic magnetic field model.

3.3. GOES Fluxes and Flare Magnitude

The GOES 1–8 Å flux is often used to characterize the flare magnitude, mostly because of the convenience of the permanent availability of GOES observations (since 1974). It

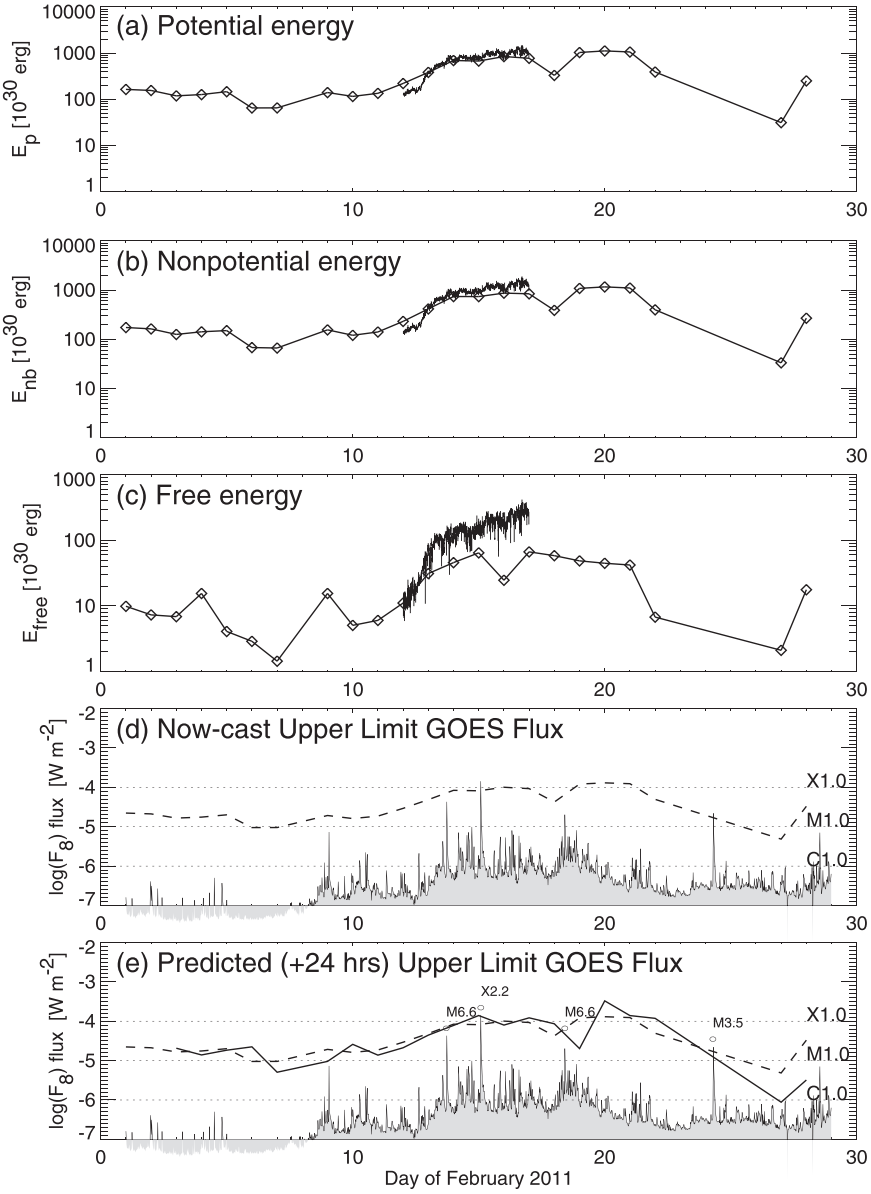

Figure 4. Time evolution of the potential field energy E_p (a), the non-potential energy $E_{\rm np}$ (b), and the free energy $E_{\rm free} = E_{\rm np} - E_p$ (c) during the month of 2011 February, with a daily cadence. The light curves (diamonds) are new calculations with the latest version of the VCA-NLFFF code, while the noisy curves with cadence of 6 minutes are taken from an older version (Aschwanden 2016). Panel (d) shows the GOES light curve (shaded with gray), with a cadence of 0.3 hr, and the now-cast upper limit of the GOES flux (dashed curve) calculated from the scaling relationship $F_8(t) \propto E_p(t)^{0.92}$. Panel (e) shows the predicted upper limit of the GOES 1–8 Å flux, extrapolated for a time window of +24 hr (solid curve), along with the now-cast predictions (dashed curve). Four observed flare events of GOES class $>M3.0$ are marked with circles, which all are close to the predicted upper limit of the GOES flux.

is therefore important to quantify how well the GOES flux correlates with other flare magnitude indicators. In this study we include large flares (of X- and M-class) only, which are the most relevant events to derive upper limits of the GOES flux, while smaller flares (of C- and B-class) are neglected here, since we are not interested in representative distribution functions, which would exhibit power laws (e.g., Aschwanden & Freeland 2012). The GOES flux appears to correlate with the upper limit of the absolute total flux near the strong-field, high-gradient polarity inversion lines (Schrijver 2007, 2009). A strong correlation has been established between the GOES flux and the thermal energy (Reep et al. 2013, 2020), or between the temperature as well as the EM of the thermal plasma and the GOES flux (Warmuth & Mann 2016a, 2016b). Even for cool (small) flares of GOES class B5 to C2, the EM was found to be correlated with the GOES flux (Phillips & Feldman 1995). Correlations between the GOES flux and the AIA/SDO or SECCHI Extreme Ultraviolet Imager (EUVI)/Solar Terrestrial Relations Observatory (STEREO) flux have been found for occulted flares (Nitta et al. 2013). However, using large statistics of 50,000 solar flares observed during three solar cycles, the exact values of GOES peak temperatures and EMs were found to depend on the background subtraction method (Ryan et al. 2012), originally pointed out by Bornmann (1990). However, for large (M- and X-class) flares, as used here, the background correction is negligible.

We have to mention the caveat that the calculation of the GOES EM and temperature from an inversion of the two-channel GOES fluxes (1–8 and 0.5–4 Å) is based on the isothermal assumption (Thomas et al. 1985; White et al. 2005),

and thus is generally not compatible when comparing different instruments, such as AIA, GOES, and RHESSI (Ryan et al. 2014). Here we find an empirical normalization factor for the EM obtained from GOES and AIA (i.e., $q_{\rm AIA} = {\rm EM_{GOES}}/{\rm EM_{AIA}} \approx 0.54$ (Equation (15)).

In summary, while all previously published studies agree that the EM is highly correlated with the GOES flux F_8 (Equation (17)), we find that the underlying CCC actually has the highest value (0.99) among all investigated correlations, and thus both the EM as well as the GOES class (flux) are equally good measures of the flare magnitude, analogously to the Gutenberg-Richter scale (or magnitude) of earthquakes.

4. Conclusions

Solar flare prediction is a highly desirable goal, as revealed by the hundreds of scientific publications highlighting it over the last decade. However, the terms "prediction" and "forecasting" have different meanings to researchers. We can distinguish between at least two different types of predictions: (i) the *deterministic* approach, which aims to predict the occurrence time and size of individual events, and (ii) the *stochastic* approach, which predicts statistical distributions only, without any temporal evolution of individual events. The deterministic approach is of course the more challenging task, because it requires an accurate and realistic physical model, while the stochastic approach just requires statistics of large samples. Extreme events are often produced by nonlinear physical mechanisms, which have the tendency to form "fat tails" in their statistical distributions in the form of power-law or log-normal functions. A popular new type of methods is "machine-learning," which is able to learn and improve predictions by optimizing parameter combinations from an initial "training data set." However, successful machine-learning can only be accomplished if the most relevant physical parameters are included in the training data set, which is essentially not available as long as we do not have knowledge of the correct physical mechanism. In this study we explore empirical scaling laws that quantify realistic parameter distributions and significant correlations of physical parameters in solar flares, which can be extrapolated into the near future and predict reliable upper limits of flare magnitudes (in terms of GOES fluxes). Our main conclusions are as follows:

1. The success of any flare prediction algorithm rests in the selection of relevant physical parameters. Since the (magnetic) potential field represents the minimum state of energy, only the free energy $E_{\rm free} = E_{\rm np} - E_p$ can be dissipated in flares, which requires knowledge of the three magnetic field components $\boldsymbol{B}_p$, $\boldsymbol{B}_{\rm np}$, and $\boldsymbol{B}_{\rm free}$. Scaling laws that do not take into account the free energy explicitly may be unphysical.
2. Another inconsistency that appeared in the extrapolation of both the potential or the non-potential magnetic field is the neglect of the photospheric non-force-freeness, a common assumption in traditional NLFFF codes. Here we bypass the non-force-freeness of the photosphere by fitting coronal loops (which are supposed to be force-free in the corona due to the low plasma-β parameter), using the VCA-NLFFF code. This may affect the magnetic field parameters and their correlations in flare scaling laws.
3. Two-parameter correlations (Figure 1) constitute a subset of simplified or approximative scaling laws, which we explore in this study. The best correlations among physical flare parameters are found for the free energy and potential field energy, $E_{\rm free} \propto E_p^{1.26}$; the dissipated energy, $E_{\rm diss} \propto E_p^{1.32}$; the magnetic flare volume, $V \propto E_{\rm diss}^{1.17}$; the (multi-)thermal energy, $E_{\rm th} \propto V_{\rm th}^{0.76}$; the EM, ${\rm EM} \propto E_{\rm th}^{0.79}$, and the GOES flux, $F_8 \propto E_p^{0.92}$. The fact that these parameters exhibit tight correlations makes them highly relevant for flare scaling laws.
4. In the opposite, uncorrelated parameters do not reveal scaling laws. This is evident, for instance, from scatterplots of the electron density n_e or the electron temperature T_e with other flare parameters, if we restrict to M- and X-class flares only. However, both the electron density and electron temperature are correlated with the GOES flux if one includes C- and B-class flares (Feldman et al. 1996). Here we restrict ourselves to large flares of X- and M-class for the prediction of the upper limits of GOES fluxes, where the EM-weighted temperature ($T_w = 25 \pm 5$ Mm) has a standard deviation of $\pm 20\%$ only. The electron density n_e has a similar small spread of less than an order of magnitude (e.g., Aschwanden 2020), while all volume-dependent flare parameters exhibit a much larger spread (some two to three order of magnitudes for X- and M-class flares), and thus dominate the two-parameter correlations.
5. Among the parameters that correlate best with the GOES flux (Figure 2), we find the EM, $F_8 \propto {\rm EM}^{1.06}$; the thermal energy, $F_8 \propto E_{\rm th}^{0.84}$; and the thermal flare volume, $F_8 \propto V_{\rm th}^{0.66}$. Comparing the observed GOES-class values ($F_8^{\rm obs}$) with the theoretically predicted values ($F_8^{\rm pred}$) based on the two-parameter scaling laws, we find a satisfactory agreement of $q_{acc} = F_8^{\rm pred}/F_8^{\rm obs} = 1.00 \pm 0.40$, after normalization of the fluxes. Thus, the accuracy of predicted GOES-class magnitudes is of the order of $\pm 40\%$ (Figure 3).
6. Our flare prediction method yields upper limits of the GOES flux $F_8^{\rm theo}(t)$, either instantaneously for now-casting (Figure 4(d)), or during time intervals of at least $\Delta t \leqslant 24$ hr (Figure 4(e)) for forecasting. The chief assumption is the slow time variability of the potential field energy $E_p(t)$ on timescales of $\leqslant$24 hr, which allows for the temporal extrapolation of the scaling law $F_8(t) \propto E_p(t)^{0.92}$ (Figure 4). We tested our forecasting method over a time interval of 28 days and validated our claim that this method yields reliable upper limits of the GOES flux. Future applications to longer time intervals with larger flare statistics will allow us also to verify the statistical probabilities of the most extreme events, which exceed the predicted upper limits, also known as "Dragon-King" events (Sornette 2009; Sornette & Ouillon 2012; Aschwanden 2019b).
7. We have to be aware that two-parameter correlations represent flare scaling laws with a minimal number of parameters, which can be refined for specific flare models (such as the Sweet–Parker or Petschek model). For instance, a Petschek-type flare model can be quantified with eight physical parameters for the dissipated flare energy, $E_{\rm MR} \propto B_{\rm free}^2 B_{\rm np} L n_e^{1/2} \lambda M_{\rm A} \tau_{\rm flare}$, with $E_{\rm MR}$ the dissipated energy, $B_{\rm free}$ the magnetic field component associated with the free energy, $B_{\rm np}$ the non-potential field strength, L the flare length scale, n_e the electron density, λ the electron density scale height, $M_{\rm A}$ the Mach

number of the magnetic reconnection outflow, and $\tau_{\rm flare}$ the flare duration (Aschwanden 2020).

The aim of this study is the distillation of the most relevant physical parameters that play a role in flare prediction methods. Once we manage this task, deterministic as well as stochastic flare prediction becomes a promising option, at least over a time interval that exhibits coherent magnetic field evolution. Future work may test the reliability of predicting upper limits for the GOES flux over the entire 10 yr interval of the SDO mission. Furthermore, various machine-learning methods applied to the most relevant physical parameters may optimize realistic scaling laws.

We thank the anonymous referee and the statistical editor for helpful comments. We acknowledge software support by Samuel Freeland, Greg Slater, and Mark Noga. Part of the work was supported by NASA contract NNG 04EA00C of the SDO/AIA instrument and the NASA STEREO mission under NRL contract N00173-02-C-2035.

Appendix
Derivation of Scaling Laws for GOES Flux

The scaling laws between the magnetic potential field energy E_p, the dissipated energy in flares $E_{\rm diss}$, the thermal flare volume $V_{\rm th}$, the (multi-)thermal flare energy $E_{\rm th}$, and the EM are specified in Equations (9), (8), (7), and (3), respectively,

$$\left(\frac{\rm EM}{10^{40}\ {\rm cm}^3}\right) = 10^{a_0}\left(\frac{E_{\rm th}}{10^{30}\ {\rm erg}}\right)^{a_1}, \quad \text{(A1)}$$

$$\left(\frac{E_{\rm th}}{10^{30}\ {\rm erg}}\right) = 10^{b_0}\left(\frac{V_{\rm th}}{10^{24}\ {\rm cm}^3}\right)^{b_1}, \quad \text{(A2)}$$

$$\left(\frac{V_{\rm th}}{10^{24}\ {\rm cm}^3}\right) = 10^{c_0}\left(\frac{E_{\rm diss}}{10^{30}\ {\rm erg}}\right)^{c_1}, \quad \text{(A3)}$$

$$\left(\frac{E_{\rm diss}}{10^{30}\ {\rm erg}}\right) = 10^{d_0}\left(\frac{E_p}{10^{30}\ {\rm erg}}\right)^{d_1}, \quad \text{(A4)}$$

with the coefficients $a_0 = 8.33$, $a_1 = 0.79$, $b_0 = -1.54$, $b_1 = 0.76$, $c_0 = 2.34$, $c_1 = 1.17$, $d_0 = -2.19$, and $d_1 = 1.32$, as determined from the linear regression fits shown in Figure 1. The scaling law of the GOES flux F_8 as a function of the EM is according to Equation (16),

$$F_8({\rm EM}) = f_0\ {\rm EM}, \qquad f_0 = q_{\rm AIA} b_8(T_w) 10^{-55}. \quad \text{(A5)}$$

The second relationship of the GOES flux $F_8(E_{\rm th})$ as a function of the thermal energy $E_{\rm th}$ is obtained by inserting Equation (A1) into Equation (A5),

$$F_8(E_{\rm th}) = f_0\ 10^{40+a_0}\left(\frac{E_{\rm th}}{10^{30}\ {\rm erg}}\right)^{a_1}. \quad \text{(A6)}$$

The third relationship of the GOES flux $F_8(V_{\rm th})$ as a function of the thermal flare volume $V_{\rm th}$ is obtained by inserting Equation (A2) into Equation (A6),

$$F_8(V_{\rm th}) = f_0\ 10^{40+a_0+b_0a_1}\left(\frac{V_{\rm th}}{10^{24}\ {\rm erg}}\right)^{a_1b_1}. \quad \text{(A7)}$$

The fourth relationship of the GOES flux $F_8(E_{\rm diss})$ as a function of the magnetic dissipated energy $E_{\rm diss}$ is obtained by inserting Equation (A3) into Equation (A7),

$$F_8(E_{\rm diss}) = f_0\ 10^{40+a_0+b_0a_1+c_0a_1b_1}\left(\frac{E_{\rm diss}}{10^{30}\ {\rm erg}}\right)^{a_1b_1c_1}. \quad \text{(A8)}$$

The fifth relationship of the GOES flux $F_8(E_p)$ as a function of the magnetic potential energy E_p is obtained by inserting Equation (A4) into Equation (A8),

$$F_8(E_p) = f_0\ 10^{40+a_0+b_0a_1+c_0a_1b_1+d_0a_1b_1c_1} \times \left(\frac{E_p}{10^{30}\ {\rm erg}}\right)^{a_1b_1c_1d_1}, \quad \text{(A9)}$$

which yields to the numerical values given in Equations (21) and (24). This scaling law stated in Equation (24) is most useful for flare prediction in terms of the GOES flux F_8 as a function of the magnetic potential field energy E_p.

ORCID iDs

Markus J. Aschwanden https://orcid.org/0000-0003-0260-2673

References

Aschwanden, M. J. 2016, ApJS, 224, 25
Aschwanden, M. J. 2019a, ApJ, 885, 49, (Paper IX)
Aschwanden, M. J. 2019b, ApJ, 880, 105
Aschwanden, M. J. 2020, ApJ, in press
Aschwanden, M. J., Boerner, P., Caspi, A., et al. 2015a, SoPh, 290, 2733
Aschwanden, M. J., Boerner, P., Ryan, D., et al. 2015b, ApJ, 802, 53, (Paper II)
Aschwanden, M. J., & Freeland, S. L. 2012, ApJ, 754, 112
Aschwanden, M. J., Sun, X., & Liu, W. 2014a, ApJ, 785, 34
Aschwanden, M. J., Xu, Y., & Jing, J. 2014b, ApJ, 797, 50, (Paper I)
Barnes, G., & Leka, K. D. 2008, ApJL, 688, L107
Barnes, G., Leka, K. D., Schrijver, C. J., et al. 2016, ApJ, 829, 89
Barnes, G., Leka, K. D., Schumer, E. A., & Della-Rose, D. J. 2007, SpWea, 5, 9
Barnes, G., Longcope, D. W., & Leka, K. D. 2005, ApJ, 629, 561
Bobra, M. G., & Couvidat, S. 2015, ApJ, 798, 135
Bobra, M. G., & Ilionidis, S. 2016, ApJ, 821, 127
Bornmann, P. L. 1990, ApJ, 356, 733
Cui, Y., Li, R., Zhang, L., et al. 2006, SoPh, 237, 45
Falconer, D. A., Abdulnasser, F., Khazanov, I., et al. 2011, SpWea, 9, S04003
Falconer, D. A., Moore, R. L., Barghouty, A. F., et al. 2012, ApJ, 757, 32
Falconer, D. A., Moore, R. L., & Gary, G. A. 2003, JGR, 108, 1380
Feldman, U., Doschek, G. A., Behring, W. E., & Phillips, K. J. H. 1996, ApJ, 460, 1034
Fleck, B., Domingo, V., & Poland, A. 1995, SoPh, 162
Freeland, S. L., & Handy, B. N. 1998, SoPh, 182, 497
Gallagher, P. T., Moon, Y. J., & Wang, H. 2002, SoPh, 209, 171
Georgoulis, M. K. 2012, SoPh, 276, 161
Georgoulis, M. K., & Rust, D. M. 2007, ApJL, 661, L109
Jonas, E., Bobra, M., Shankar, V., et al. 2018, SoPh, 293, 48
Leka, K. D., & Barnes, G. 2003, ApJ, 595, 1277
Leka, K. D., & Barnes, G. 2007, ApJ, 656, 1173
Lemen, J. R., Duncan, D., Edwards, C., et al. 2004, Proc. SPIE, 5171, 65
Lemen, J. R., Title, A. M., Akin, D. J., et al. 2012, SoPh, 275, 17
Mason, J. P., & Hoeksema, J. T. 2010, ApJ, 723, 634
Metcalf, T. R., Litao, J., McClymont, A. N., & Canfield, R. C. 1995, ApJ, 439, 474
Nishizuka, N., Sugiura, K., Kubo, Y., et al. 2017, ApJ, 835, 156
Nitta, N. V., Aschwanden, M. J., Boerner, P. F., et al. 2013, SoPh, 288, 241
Pesnell, W. D., Thompson, B. J., & Chamberlin, P. C. 2012, SoPh, 275, 3
Phillips, K. J. H., & Feldman, U. 1995, A&A, 304, 563
Priest, E. R. 1975, SoPh, 43, 177
Reep, J. W., Antolin, P., Bradshaw, S. J., et al. 2020, ApJ, 890, 100
Reep, J. W., Bradshaw, S. J., & McAteer, R. T. J. 2013, ApJ, 778, 76
Ryan, D. F., Gallather, P. T., Dennis, B. R., et al. 2012, ApJSS, 202, 11

Ryan, D. F., O'Flannagaink, A. M., Aschwanden, M. J., & Gallagher, P. T. 2014, SoPh, 289, 2547
Scherrer, P. H., Bogart, R. S., Bush, R. I., et al. 1995, SoPh, 162, 129
Scherrer, P. H., Schou, J., & Bush, R. J. 2012, SoPh, 275, 207
Schrijver, C. J. 2007, ApJL, 655, L117
Schrijver, C. J. 2009, AdSpR, 43, 739
Sornette, D. 2009, J. Terraspace Science and Engeneering, 2, 1
Sornette, D., & Ouillon, G. 2012, EPJST, 205, 1
Thomas, R. J., Starr, R., & Crannell, C. J. 1985, SoPh, 95, 323
Tiwari, S. K., Venkatakrishnan, P., Gosein, S., et al. 2010, ApJ, 721, 622
Warmuth, A., & Mann, G. 2016a, A&A, 588, A115
Warmuth, A., & Mann, G. 2016b, A&A, 588, A116
Welsch, B. T., Li, Y., Schuck, P. W., & Fisher, G. H. 2009, ApJ, 705, 821
White, S. M., Thomas, R. J., & Schwartz, R. A. 2005, SoPh, 227, 231
Wiegelmann, T., Inhester, B., & Sakurai, T. 2006, SoPh, 223, 215